Chlorine-Enabled Electron Doping in Solution-Synthesized SnSe Thermoelectric Nanomaterials

*Guang Han, Srinivas R. Popuri, Heather F. Greer, Lourdes F. Llin, Jan-Willem G. Bos, Wuzong Zhou, Douglas J. Paul, Hervé Ménard, Andrew R. Knox, Andrea Montecucco, Jonathan Siviter, Elena A. Man, Wen-guang Li, Manosh C. Paul, Min Gao, Tracy Sweet, Robert Freer, Feridoon Azough, Hasan Baig, Tapas K. Mallick, and Duncan H. Gregory**

An aqueous solution method is developed for the facile synthesis of Cl-containing SnSe nanoparticles in 10 g quantities per batch. The particle size and Cl concentration of the nanoparticles can be efficiently tuned as a function of reaction duration. Hot pressing produces n-type Cl-doped SnSe nanostructured compacts with thermoelectric power factors optimized via control of Cl dopant concentration. This approach, combining an energy-efficient solution synthesis with hot pressing, provides a simple, rapid, and low-cost route to high performance n-type SnSe thermoelectric materials.

Doping plays a vital role in modifying the electronic properties of semiconductors and is pivotal for (opto)electronics,[1] photovoltaics (PV),[2] and thermoelectrics.[3] Metal chalcogenides (MCs) form a diversity of functional materials well-suited to such applications. Halogen doping in MCs has proven effective to realize n-type conducting behavior and tune carrier concentrations.[2–4] Enhanced thermoelectric and PV performance can result.[2–4] While halogens can be readily doped into bulk MCs by high-temperature synthesis using metal halide precursors,[4] doping proves challenging for solution-synthesized MC nanostructures.[5] Recently, post-synthesis halide treatment of nanocrystals in solution has been developed which involves switching halogens for long chain surfactant molecules absorbed on the surface.[2,6] In fact, sorption of halogens can be realized as part of a one-pot synthesis using metal halide precursors.[7] Although this strategy was initially developed for passivation of MC quantum dots against oxidation,[2,6,7] annealing or hot pressing halogen-coated nanoparticles allows halides to diffuse into the MC lattice and substitute for chalcogenide anions.[8] However, controlling doping levels is not straightforward and such methods can introduce rather high halide concentrations in small nanocrystals leading to reduced electrical conductivity.[8b] Hence exerting control over dopant concentration without sacrificing electrical performance is imperative.

Thermoelectrics realize direct interconversion between thermal and electric energy, thus providing an important route

Dr. G. Han, Prof. D. H. Gregory
WestCHEM
School of Chemistry
University of Glasgow
Glasgow G12 8QQ, UK
E-mail: Duncan.Gregory@glasgow.ac.uk
Dr. S. R. Popuri, Dr. J.-W. G. Bos
Institute of Chemical Sciences and Centre for Advanced Energy Storage and Recovery
School of Engineering and Physical Sciences
Heriot-Watt University
Edinburgh EH14 4AS, UK
Dr. H. F. Greer, Prof. W. Z. Zhou
EaStCHEM
School of Chemistry
University of St Andrews
St Andrews, Fife KY16 9ST, UK
Dr. L. F. Llin, Prof. D. J. Paul, Prof. A. R Knox, Dr. A. Montecucco, Dr. J. Siviter, Dr. E. A. Man, Dr. W.-g. Li, Dr. M. C. Paul
School of Engineering
University of Glasgow
Glasgow G12 8QQ, UK
Dr. H. Ménard
Sasol (UK) Ltd
St Andrews, Fife KY16 9ST, UK
Prof. M. Gao, Dr. T. Sweet
School of Engineering
Cardiff University
Cardiff CF24 3AA, UK
Prof. R. Freer, Dr. F. Azough
School of Materials
University of Manchester
Manchester M13 9PL, UK
Dr. H. Baig, Prof. T. K. Mallick
Environment and Sustainability Institute
University of Exeter
Penryn Campus, Penryn TR10 9FE, UK

DOI: 10.1002/aenm.201602328

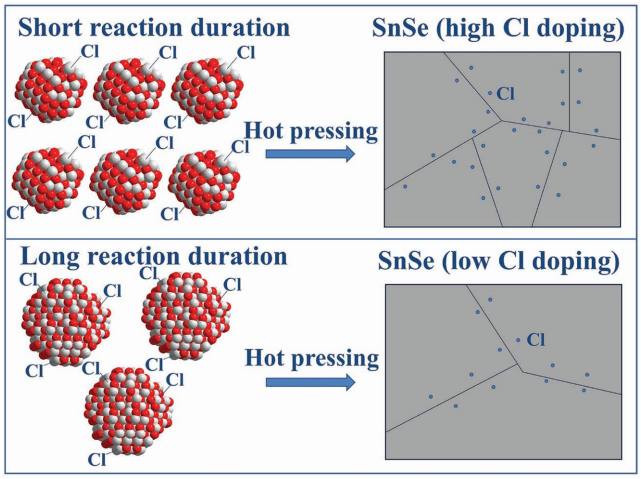

Scheme 1. The strategy to fabricate n-type SnSe nanostructured pellets utilizes Cl concentration and nanoparticle size from solution-synthesis.

to produce useful electricity from waste heat and to perform refrigeration (via the Seebeck and Peltier effects, respectively).[9] SnSe is a layer-structured MC semiconductor and potentially useful thermoelectric material given its excellent energy conversion efficiency, relatively low toxicity, and the high earth-abundance of the component elements.[10] Most research to date has concentrated on p-type SnSe.[10,11] Conversely n-type SnSe is difficult to achieve; only I and $BiCl_3$ have been used successfully to dope bulk SnSe with electrons. Moreover, high-temperature, energy-intensive processes are needed to achieve this.[12] There are no reports of solution-synthesized SnSe nanostructures with tunable n-type conducting behavior. Before the potential of SnSe can be fully realized, it is critical to develop a cost-effective and large-scale synthesis of high performing n-type SnSe, to complement existing p-type materials.

In this study, we demonstrate the introduction of Cl to SnSe nanoparticles by a one-pot in situ solution approach to prepare >10 g of doped SnSe nanoparticles on short timescales (**Scheme 1**; Figure S1, Supporting Information). The strategy exploits the nucleophilic nature of the halide anion and the electrophilicity of coordinatively unsaturated metal cations at the nanoparticle surface,[6] coupled with the acidic conditions that promote the formation of metal–halide bonds by ligand replacement.[8a] The simple solution synthesis is achieved using aqueous $SnCl_2$ both as reactant and Cl source and citric acid both as surfactant to restrict particle growth and means to control pH. Controlling the reaction duration allows us to engineer nanoparticle size and regulate the Cl dopant level. The nanoparticles can be hot-pressed into Cl-doped SnSe dense pellets with controllable dopant concentration and consistent n-type conducting behavior.

Injection of an NaHSe aqueous solution into an $SnCl_2$ solution (26:1 molar ratio of citric acid:$SnCl_2$) leads to the immediate formation of an SnSe precipitate (Equation (1))

$$NaHSe + SnCl_2 \rightarrow SnSe + NaCl + HCl \quad (1)$$

Boiling the suspension for 2 h generates crystalline, phase-pure SnSe nanoparticles. Powder X-ray diffraction (PXD) patterns can be exclusively indexed to orthorhombic SnSe (ICDD card No. 48–1224).[13] Rietveld refinement against PXD data (**Figure 1**a; Tables S1 and S2, Supporting Information) confirms that the single phase SnSe product crystallizes in orthorhombic space group *Pnma*, with a = 11.5424(8) Å, b = 4.1775(4) Å, and c = 4.3841(5) Å. Scanning electron microscopy (SEM) images (Figure S2a,b, Supporting Information) reveal that the product is an agglomeration of nanoparticles with individual sizes of 15–55 nm. Energy dispersive X-ray spectroscopy (EDS) spectra (Figure S2c, Supporting Information) taken across the samples as point and area scans consistently generate Sn:Se:Cl atomic ratios of 50.6(5):48.8(5):0.6(1). The existence of Cl should result from the interaction of nucleophilic Cl^- and electrophilic Sn^{2+}

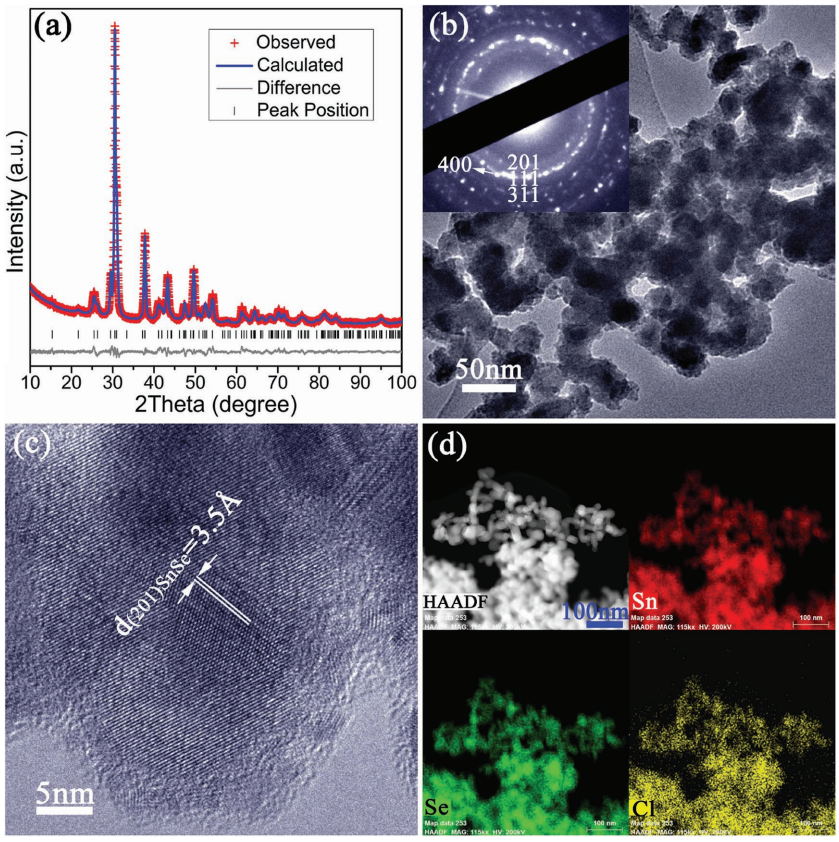

Figure 1. Characterization of SnSe nanoparticles synthesized after 2 h. a) Profile plot from Rietveld refinement against PXD data. b) TEM image and corresponding SAED pattern collected from the nanoparticles. c) HRTEM image of an individual nanoparticle with the (201) *d*-spacing indicated. d) EDS mapping of a nanoparticle cluster. The four panels in (d) are (clockwise from top left) high angle annular dark field (HAADF) image, elemental mapping for Sn (red), Cl (yellow), and Se (green).

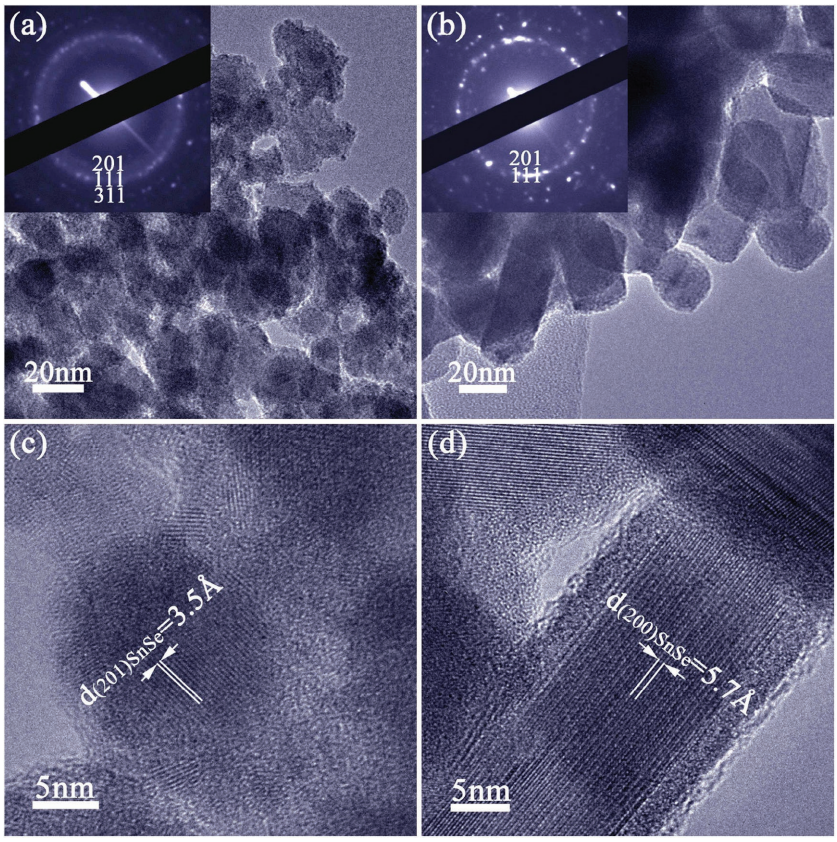

Figure 2. TEM characterization of SnSe nanoparticles synthesized after a,c) 1 min and b,d) 24 h. a,b) TEM images and corresponding SAED patterns collected from the particles. c,d) HRTEM images of individual nanoparticles with selected *d*-spacings indicated.

at the nanoparticle surface[6] together with the replacement of ligated citric acid by Cl^- in the acidic environment during solution heating.[8a] Transmission electron microscopy (TEM) images (Figure 1b; Figure S2d, Supporting Information) confirm that SnSe nanoparticles assemble into clusters with an average individual particle size of ≈35 nm. Selected area electron diffraction (SAED) patterns (Figure 1b) collected from a section of such a cluster reveal the polycrystalline nature of the SnSe particles. High-resolution TEM (HRTEM) images (Figure 1c) nevertheless demonstrate the single crystalline nature of individual nanoparticles. Elemental mapping (Figure 1d) confirms the existence and uniform distribution of Sn, Se, and Cl in the nanoparticles.

Controlling the synthesis duration can predetermine both the particle size and Cl content of the SnSe nanoparticles. To illustrate this, we synthesized materials from 1 min, 5 min, and 24 h of solution heating. PXD (Figures S3 and S4; Table S1, Supporting Information) reveals each product to be single-phase with the orthorhombic SnSe structure. The refined cell volumes increase slightly with reaction time and the Bragg half-widths decrease gradually as the reaction duration increases, indicating likely crystallite growth. SEM (Figure S5a–f, Supporting Information) and TEM (**Figure 2**a,b: Figure S6a, Supporting Information) images show that the products are composed of nanoparticles, and the average particle size increases from ≈25 nm through ≈30 to ≈50 nm, as heating is extended. EDS (Figure S5g–i, Supporting Information) confirms the existence of Cl in all the samples and shows increased Cl levels for shorter reaction times; specifically, the Sn:Se:Cl atomic ratios are 48.2(5):50.5(5):1.3(2), 51.6(5):47.7(5):0.7(1), and 51.5(5):48.2(5):0.3(1) for nanoparticles synthesized after 1 min, 5 min, and 24 h, respectively. SAED patterns (Figure 2a,b; Figure S6b, Supporting Information) confirm the polycrystalline nature of the SnSe nanoparticles. Furthermore, HRTEM (Figure 2c; Figure S6c,d, Supporting Information) reveals that the products synthesized after 1 and 5 min have relatively poor crystallinity, and nanoparticles with sizes of 2–4 nm are attached on the surface of larger particles. When the reaction time is increased from 2 to 24 h (Figure 2d), individual particles become single crystalline. This suggests that the aggregation and coalescence of small nanoparticles leads to the formation of larger single crystalline nanoparticles.[14]

The ability to prepare SnSe nanomaterials in >10 g quantities allowed the facile fabrication of SnSe pellets via hot pressing without the variations in sample morphology that could ensue from repeated sample preparation. Pellets with ≈95% of the SnSe theoretical density, consolidated from 2 h solution-synthesized powder, were obtained (denoted **1**). Rietveld refinement (Figure S7; Table S3, Supporting Information) shows that the pellets are composed principally of orthorhombic SnSe (79.1(1) wt%) but also of two minority phases of trigonal $SnSe_2$ (11.1(3) wt%) and tetragonal SnO_2 (9.8(2) wt%). This indicates that a small proportion of SnSe was oxidized to SnO_2 and $SnSe_2$ during the hot pressing process ($2SnSe + O_2 \rightarrow SnO_2 + SnSe_2$). A series of subsequent experiments (see Figures S8–S15; Tables S4–S6, Supporting Information) confirmed that the oxidation was less in nanomaterials prepared at longer reaction durations. Both particle size (and by inference surface area) and the relative amount of surface carboxyl groups could be traced as contributors to the oxidation process.

Preferred orientation of both SnSe and $SnSe_2$ crystallites is evidenced by the increased intensity of the (*h*00) and (00*l*) reflections respectively in PXD patterns from the pellets (Figure S16, Supporting Information). This suggests that the longest crystallographic axes of the respective cells align parallel to the hot pressing direction. Considering that the magnitude of the electrical conductivity is highest perpendicular to these long axes in both SnSe and $SnSe_2$,[10a,15] such an orientation should be beneficial in enhancing electrical conductivity perpendicular to the hot pressing direction of the pellets.

SEM and TEM images (Figure S17a,b and S18a, Supporting Information) show that **1** is composed of densely packed plates with almost uniformly distributed particles. EDS (Figure S17c–g, Supporting Information) confirms the existence and uniform distribution of Cl in **1**. SAED patterns (Figure S18b, Supporting

Table 1. A summary of Cl concentration, phase fraction, electrical properties, n–p transformation temperature, room temperature Hall carrier concentration (n_H), and mobility (μ_H) of the pellets.

Pellet	at% Cl	$S_{300\,K}$ [$\mu V\,K^{-1}$]	$\sigma_{300\,K}$ [$S\,m^{-1}$]	T_{n-p} [K]	wt% SnO_2	wt% $SnSe_2$	n_H [$10^{18}\,cm^{-3}$]	μ_H [$cm^2\,V^{-1}\,s^{-1}$]
1	0.6(1)	−265	255	–[a)]	9.8(2)	11.1(3)	6.43	3.60
3	0.7(1)	−295	185	–[a)]	13.0(2)	15.3(3)	3.47	2.66
4	0.3(1)	−145	55	475	3.5(2)	6.1(2)	2.56	0.85
SF1	0.3(1)	−175[b)]	55[b)]	520	7.9(1)	6.7(2)	1.68	2.14
SF2	0.1(1)	−95[b)]	50[b)]	400	5.5(1)	6.8(2)	1.24	1.62

[a)]No transition below 550 K; [b)]Values obtained at 325 K.

Information) taken from a number of plates and nanoparticles from **1** confirm the presence of the above-mentioned three phases: SnSe, $SnSe_2$, and SnO_2. HRTEM images demonstrate that the predominant plate-like structures in **1** are crystalline SnSe (Figure S18c, Supporting Information). High-resolution images also show that some of the smaller irregular nanoplates are formed by $SnSe_2$ (Figure S18d, Supporting Information) while some nanoparticles of SnO_2 are distributed among the SnSe plates (Figure S18e, Supporting Information). Thermogravimetric-differential thermal analysis of **1** under argon (Figure S19, Supporting Information) shows negligible weight loss below 500 °C, but reveals that decomposition begins above this temperature and corresponds to an endothermic Se sublimation process.

For comparison, the nanomaterials prepared over 1 min, 5 min, and 24 h were also hot pressed into pellets (denoted **2**, **3**, **4**, respectively) using the same processing parameters, achieving ≈85%, ≈90%, and ≈92% of the SnSe theoretical density, respectively. Rietveld refinement against PXD data (Figure S20; Tables S7–S9, Supporting Information) shows that the SnSe phase fraction increases from ≈71 through 72 to 90 wt% for **2**, **3**, and **4**, respectively, again indicating a direct correlation between synthesis time (and particle size/surface citric acid amount) and the tendency to oxidation. HRTEM on **3** confirms that SnO_2 nanoparticles are distributed in close proximity to the SnSe plates (Figure S21, Supporting Information). EDS (Figure S22, Supporting Information) confirms that the pellets contain Cl at levels consistent with the corresponding solution synthesized SnSe nanoparticles, suggesting no loss during the hot pressing process. X-ray photoelectron spectroscopy (XPS) was used to verify the presence of chlorine and analysis of **3** (Figure S23, Supporting Information) shows that the peaks at 200.5 and 198.9 eV can be assigned to Cl $2p_{1/2}$ and Cl $2p_{3/2}$ states, respectively, indicating that Cl exists in the form of Cl^-.[7a,16] This implies electron doping indeed originates from the halide on substitution for Se^{2-}.[16] The indirect optical bandgap from diffuse reflectance (DR) UV–Vis spectra (Figure S24, Supporting Information) narrows from ≈0.8 through ≈0.75 to ≈0.7 eV, when the Cl concentration is increased from ≈0.3% (**4**) through ≈0.7%–0.6% (**3**, **1**) to ≈1.3% (**2**), respectively. This insinuates that the indirect bandgap of SnSe is reduced slightly but significantly by increased Cl doping. A similar bandgap narrowing was observed in I-doped SnSe and is expected to improve the electrical conductivity in SnSe.[12a]

We selected **1**, **3**, and **4** for electrical measurements due to the relatively low percentage of SnO_2 and $SnSe_2$ components and the high density achieved (≥90%). Hall measurements (**Table 1**) give a clear correlation between the Cl and carrier concentrations (where the majority carriers are electrons). **1** and **3** have higher carrier concentrations than **4** due to the twofold increase in Cl content, while **3** has a lower carrier concentration than **1**, which is probably related to the higher level of impurities. The contrast in the temperature-dependent Seebeck coefficient (S) for the different pellets is striking (**Figure 3**a; Table 1). The variation in the absolute value of S with temperature for **1** and **3** is very similar increasing from 300 K to reach a maximum at ≈410–425 K before decreasing by 540 K. The decreasing value of S at higher temperature could be due to thermal excitation of minority carriers (holes) that are related to intrinsic defects in SnSe (e.g., Sn vacancies)[17] as manifested by the significantly enhanced electrical conductivity (Figure 3b). The absolute value of **1** is slightly lower than that of **3** at 300 K, but S for both **1** and **3** are negative within the whole temperature range, indicating n-type behavior consistent with Cl doping. By comparison, **4**, with the lowest Cl doping level, shows n-type behavior at 300 K and transforms to p-type behavior at ≈475 K with $S \approx 75\ \mu V\,K^{-1}$ at 540 K. The n- to p-type transition could also be related to the thermal excitation of holes at high temperature. We also note that the impurity phases, $SnSe_2$ and SnO_2, are both intrinsic n-type semiconductors.[16,18]

The electrical conductivity (σ) of **1** (Figure 3b) increases from ≈255 $S\,m^{-1}$ at 300 K to ≈910 $S\,m^{-1}$ at 540 K. With a similar Cl doping concentration and indirect bandgap to **1**, the σ of **3** is slightly lower (from ≈185 $S\,m^{-1}$ at 300 K to ≈685 $S\,m^{-1}$ at 540 K), probably due to the increase in the less conductive $SnSe_2$ and SnO_2 components,[16,18b] together with the increased carrier scattering from SnO_2 nanoparticles. This is consistent with the higher carrier concentration and mobility in **1** (Table 1). By contrast, with the lowest Cl doping level, **4** exhibits the lowest carrier concentration and σ among the three pellets, although it is the least oxidized. In fact, **1** and **3** demonstrate higher σ values than bulk I-doped SnSe materials with similar doping concentrations within the same temperature range (e.g., σ for $SnSe_{0.98}I_{0.02}$ increased from ≈0.23 $S\,m^{-1}$ at 300 K to ≈105 $S\,m^{-1}$ at 565 K) and comparable σ to Bi and Cl codoped materials (e.g., $SnSe_{0.95}$-0.2 mol% $BiCl_3$ yielded σ values of ≈1170 $S\,m^{-1}$ at 300 K and ≈1815 $S\,m^{-1}$ at 560 K).[12]

In an attempt to understand the possible origins of the n-type conducting behavior more fully, we also measured the

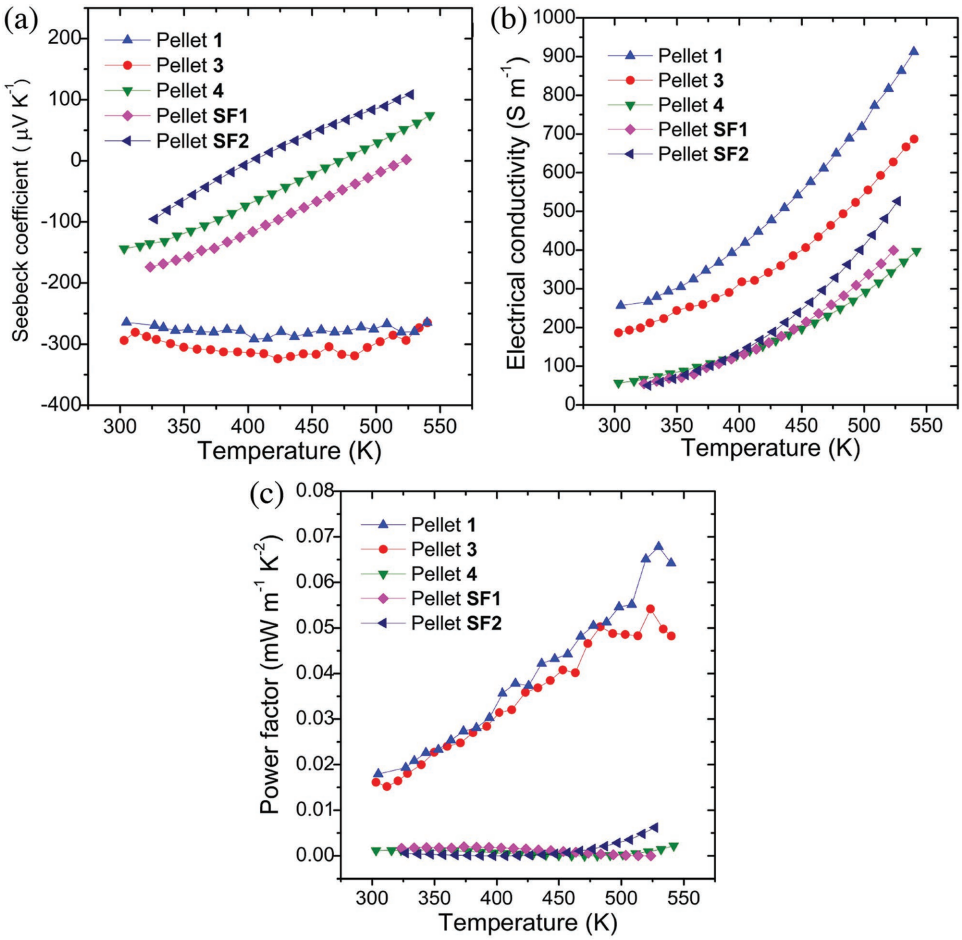

Figure 3. Electrical properties of SnSe pellets **1**, **3**, **4**, **SF1**, and **SF2** measured perpendicular to the hot pressing direction: a) the Seebeck coefficient, b) the electrical conductivity, and c) the power factor as a function of temperature.

thermoelectric performance of two pellets synthesized using hydrochloric acid in place of citric acid (**SF1** and **SF2**; see Supporting Information) for comparison (Figure 3; Table 1). EDS shows that these surfactant-free samples have larger particle size and lower Cl concentrations compared to their citric acid "analogues," **1** and **4**. (The Sn:Se:Cl ratios are 51.7(5):48.0(5):0.3(1) and 51.5(5):48.4(5):0.1(1) for **SF1** and **SF2**, respectively; Figure S14, Supporting Information). Three notable comparisons can be made: (1)**SF2** contains slightly more SnO_2 and $SnSe_2$ than **4** but contains less dopant Cl. **SF2** has a lower room temperature carrier concentration and σ, slightly lower magnitude Seebeck coefficient and transforms from n- to p-type at a lower temperature than **4**; (2) **SF1** has a similar Cl concentration but notably contains more SnO_2 than **4**. **SF1** transforms from n- to p-type at a higher temperature than **4**; (3) **1** and **3** remain n-type below 550 K with similar Seebeck coefficients, although the electrical conductivity of **1** is higher than **3**. Although there are likely to be other contributing factors, the results indicate that as Cl doping levels increase so does the electrical conductivity and the temperature of the p–n transition, both observations being consistent with a higher number of negative charge carriers. Nevertheless, the presence of SnO_2 (and $SnSe_2$) clearly also has an effect on the electrical properties, apparently reducing the conductivity and increasing the temperature of the n–p transition. These observations would certainly be consistent with the presence of SnO_2 as a wide band gap, n-type semiconductor (E_g = 3.6 eV; typically $\sigma \geq 4$ S m^{-1}, $S \approx -200$ μV K^{-1} at ≈300 K, depending on oxygen vacancy concentration).[18] ($SnSe_2$ has a gap of 1.6 eV,[19] σ of ≈170 S m^{-1},[16] $S \approx -238$ μV K^{-1} at ≈300 K.[20]) Moreover, controlled doping of Cl^- is clearly very effective in producing high performance n-type SnSe, but oxide impurities need to be minimized to optimize this performance. It is also worth noting that the absence of surfactant in the preparation of **SF1** and **SF2** ultimately leads to significant improvements in σ, especially at higher temperature (cf. **4**).[11d]

The combination of better σ values coupled with high values of S leads to higher power factors ($S^2\sigma$) in **1** (≈0.018 mW m^{-1} K^{-2} at 300 K to ≈0.068 mW m^{-1} K^{-2} at 530 K) (Figure 3c). **3** shows slightly lower values than **1** ($S^2\sigma \approx$ 0.016 mW m^{-1} K^{-2} at 300 K and ≈0.054 mW m^{-1} K^{-2} at 525 K) as noted above. In contrast, the $S^2\sigma$ values for **4** are much lower (≈0.001 mW m^{-1} K^{-2} at 300 K and reaching only ≈0.002 mW m^{-1} K^{-2} at 540 K). **SF1** and **SF2** achieve similar $S^2\sigma$ values at room temperature where they are both n-type, whereas **SF2** has a higher power factor at 525 K (where it is p-type). The contrast in performance between samples underscores the importance of being able to tune the

degree of Cl doping and to control the pellet phase composition during fabrication. It is especially notable that the power factor for **1** compares very favorably with those for I-doped SnSe (e.g., $SnSe_{0.98}I_{0.02}$, with $S^2\sigma$ of ≈0.016 mW m^{-1} K^{-2} at 565 K) and co-doped SnSe (e.g., $SnSe_{0.95}$-0.2 mol% $BiCl_3$, with an $S^2\sigma$ of ≈0.104 mW m^{-1} K^{-2} at 515 K) bulk materials with similar doping levels within the same temperature range.[12] If oxidation could be reduced, it might conceivable to surpass such values. Hence, it is achievable to produce high performing n-type SnSe materials in bulk quantities via energy-efficient, sustainable methods (Figure S25, Supporting Information). In principle, it should be possible to produce new co-doped SnSe nanomaterials controllably (e.g., with both Bi- and Cl-dopants among others) with only minor adaptations to the present synthesis method.

Preliminary thermal conductivity measurements (κ) performed on **1** and **4** along the direction parallel to pressing (Figure S26, Supporting Information) are also encouraging. κ for **1** (**4**) decreases from ≈0.89 (≈0.72) W m^{-1} K^{-1} at 300 K to ≈0.62 (≈0.40) W m^{-1} K^{-1} at 540 K. The higher κ for **1** could be due to its higher percentage of more thermally conductive SnO_2. However, κ values for both **1** and **4** are still relatively low compared to other examples of n-type polycrystalline SnSe and to p-type single crystals (Figure S26d,e, Supporting Information). This could be due to enhanced phonon scattering either from the SnO_2 nanoinclusions in these materials or as a result of the nanostructuring of SnSe itself.

In summary, a simple, quick, low-cost solution synthesis produces Cl-containing SnSe nanoparticles in gram quantities (>10 g per run for a 2 h growth). Such nanoparticles have been consolidated into n-type Cl-doped SnSe nanostructured pellets, whose thermoelectric power factors can be significantly improved by optimizing the Cl doping level. This study not only provides a convenient method for the large-scale synthesis of SnSe nanostructures, but also demonstrates a facile and reliable route to engineer n-type SnSe with well-defined doping concentration. Considering also that p-type SnSe can be synthesized by a very similar method,[11d] the way is clear toward a unified, cost-effective processing route to large quantities of both the constituent materials needed for a thermoelectric device.

Experimental Section

Full experimental details are provided in the Supporting Information.

Materials Synthesis: 260 mmol citric acid and 10 mmol $SnCl_2{\cdot}2H_2O$ were added into 50 mL deionized water (DIW) to yield a transparent solution that was heated to boil. 50 mL of freshly prepared $NaHSe_{(aq)}$ was promptly injected into the boiling solution. The solution was boiled for 2 h and cooled to room temperature under $Ar_{(g)}$ on a Schlenk line. The products were washed with DIW and ethanol and dried at 50 °C for 12 h. Scaled-up syntheses were performed with 5.5-fold precursor concentrations. The yield was 96(1)% of theoretical production. To tune the particle size and Cl level, samples synthesized over 1 min, 5 min, or 24 h durations were also prepared. For the surfactant-free synthesis, 4 mL hydrochloric acid was introduced into $SnCl_2$ solution in place of citric acid. Pellets were pressed in a graphite die under Ar (uniaxial pressure of ≈60 MPa; 500 °C; 20 min).

Materials Characterization and Testing: PXD data were recorded by a PANalytical X'pert Pro MPD diffractometer in Bragg-Brentano geometry (Cu Kα_1 radiation, λ = 1.5406 Å). Rietveld refinement was performed against PXD data using the GSAS and EXPGUI software packages.[21] Imaging and elemental analysis were performed by SEM (Carl Zeiss Sigma, at 5 and 20 kV, respectively) equipped with EDS (Oxford Instruments X-Max 80). Further imaging, elemental analysis and SAED were conducted by TEM (FEI Titan Themis 200 and JEOL JEM-2011, operated at 200 kV). Optical bandgaps were measured by DR-UV–Vis spectroscopy (Shimadzu, UV-2600). The Seebeck coefficient and electrical conductivity of pellets were measured using a Linseis LSR-3 instrument from 300 to 540 K. Thermal diffusivity (D) of pellets was measured using a Linseis LFA 1000 instrument within the same temperature range and thermal conductivity (κ) was calculated using $\kappa = DC_p\rho$, where C_p and ρ are specific heat capacity and density, respectively. Hall measurements were performed on a nanometrics HL5500 Hall system using a Van der Pauw configuration. The XPS experiments were performed using a Kratos Axis Ultra-DLD photoelectron spectrometer with an Al monochromatic X-ray source.

Supporting Information

Supporting Information is available from the Wiley Online Library or from the author.

Acknowledgements

This work was financially supported by the EPSRC (EP/K022156/1). The authors thank Peter Chung for assistance with SEM and Jialu Chen for assistance with TEM elemental mapping. S.R.P. and J.-W.G.B. acknowledge the EPSRC for support (EP/N01717X/1). H.F.G. and W.Z. acknowledge the EPSRC for the Equipment Grant to purchase Titan Themis 200 microscope (EP/L017008/1).

Received: October 21, 2016
Revised: January 5, 2017
Published online: February 20, 2017

[1] a) X. F. Duan, Y. Huang, Y. Cui, J. F. Wang, C. M. Lieber, *Nature* **2001**, *409*, 66; b) S. J. Oh, C. Uswachoke, T. S. Zhao, J. H. Choi, B. T. Diroll, C. B. Murray, C. R. Kagan, *ACS Nano* **2015**, *9*, 7536.
[2] D. Zhitomirsky, M. Furukawa, J. Tang, P. Stadler, S. Hoogland, O. Voznyy, H. Liu, E. H. Sargent, *Adv. Mater.* **2012**, *24*, 6181.
[3] a) J.-S. Rhyee, K. Ahn, K. H. Lee, H. S. Ji, J.-H. Shim, *Adv. Mater.* **2011**, *23*, 2191; b) G. Han, Z.-G. Chen, J. Drennan, J. Zou, *Small* **2014**, *10*, 2747.
[4] a) L. D. Zhao, S. H. Lo, J. Q. He, H. Li, K. Biswas, J. Androulakis, C. I. Wu, T. P. Hogan, D. Y. Chung, V. P. Dravid, M. G. Kanatzidis, *J. Am. Chem. Soc.* **2011**, *133*, 20476; b) Q. Zhang, Y. C. Lan, S. L. Yang, F. Cao, M. L. Yao, C. Opeil, D. Broido, G. Chen, Z. F. Ren, *Nano Energy* **2013**, *2*, 1121; c) H. Wang, Y. Z. Pei, A. D. LaLonde, G. J. Snyder, *Proc. Natl. Acad. Sci. USA* **2012**, *109*, 9705; d) A. D. LaLonde, Y. Z. Pei, G. J. Snyder, *Energy Environ. Sci.* **2011**, *4*, 2090.
[5] H. Fang, Z. Luo, H. Yang, Y. Wu, *Nano Lett.* **2014**, *14*, 1153.
[6] J. Tang, K. W. Kemp, S. Hoogland, K. S. Jeong, H. Liu, L. Levina, M. Furukawa, X. H. Wang, R. Debnath, D. K. Cha, K. W. Chou, A. Fischer, A. Amassian, J. B. Asbury, E. H. Sargent, *Nat. Mater.* **2011**, *10*, 765.
[7] a) J. B. Zhang, J. B. Gao, E. M. Miller, J. M. Luther, M. C. Beard, *ACS Nano* **2014**, *8*, 614; b) Z. Zhang, C. Liu, X. J. Zhao, *J. Phys. Chem. C* **2015**, *119*, 5626.
[8] a) M. Ibáñez, R. J. Korkosz, Z. S. Luo, P. Riba, D. Cadavid, S. Ortega, A. Cabot, M. G. Kanatzidis, *J. Am. Chem. Soc.* **2015**, *137*,

4046; b) D. James, X. Lu, A. C. Nguyen, D. Morelli, S. L. Brock, *J. Phys. Chem. C* **2015**, *119*, 4635.
[9] a) G. J. Tan, L. D. Zhao, M. G. Kanatzidis, *Chem. Rev.* **2016**, *116*, 12123; b) W. G. Zeier, A. Zevalkink, Z. M. Gibbs, G. Hautier, M. G. Kanatzidis, G. J. Snyder, *Angew. Chem., Int. Ed.* **2016**, *55*, 6826; c) G. J. Snyder, E. S. Toberer, *Nat. Mater.* **2008**, *7*, 105.
[10] a) L. D. Zhao, S. H. Lo, Y. S. Zhang, H. Sun, G. J. Tan, C. Uher, C. Wolverton, V. P. Dravid, M. G. Kanatzidis, *Nature* **2014**, *508*, 373; b) L.-D. Zhao, G. Tan, S. Hao, J. He, Y. Pei, H. Chi, H. Wang, S. Gong, H. Xu, V. P. Dravid, C. Uher, G. J. Snyder, C. Wolverton, M. G. Kanatzidis, *Science* **2015**, *351*, 141; c) K. Peng, X. Lu, H. Zhan, S. Hui, X. Tang, G. Wang, J. Dai, C. Uher, G. Wang, X. Zhou, *Energy Environ. Sci.* **2016**, *9*, 454.
[11] a) E. K. Chere, Q. Zhang, K. Dahal, F. Cao, J. Mao, Z. Ren, *J. Mater. Chem. A* **2016**, *4*, 1848; b) T.-R. Wei, G. Tan, X. Zhang, C.-F. Wu, J.-F. Li, V. P. Dravid, G. J. Snyder, M. G. Kanatzidis, *J. Am. Chem. Soc.* **2016**, *138*, 8875; c) C. L. Chen, H. Wang, Y. Y. Chen, T. Day, G. J. Snyder, *J. Mater. Chem. A* **2014**, *2*, 11171; d) G. Han, S. R. Popuri, H. F. Greer, J. W. G. Bos, W. Z. Zhou, A. R. Knox, A. Montecucco, J. Siviter, E. A. Man, M. Macauley, D. J. Paul, W. G. Li, M. C. Paul, M. Gao, T. Sweet, R. Freer, F. Azough, H. Baig, N. Sellami, T. K. Mallick, D. H. Gregory, *Angew. Chem., Int. Ed.* **2016**, *55*, 6433; e) S. R. Popuri, M. Pollet, R. Decourt, F. D. Morrison, N. S. Bennett, J. W. G. Bos, *J. Mater. Chem. C* **2016**, *4*, 1685; f) Y.-X. Chen, Z.-H. Ge, M. Yin, D. Feng, X.-Q. Huang, W. Zhao, J. He, *Adv. Funct. Mater.* **2016**, *26*, 6836.
[12] a) Q. Zhang, E. K. Chere, J. Y. Sun, F. Cao, K. Dahal, S. Chen, G. Chen, Z. F. Ren, *Adv. Energy Mater.* **2015**, *5*, 1500360; b) X. Wang, J. T. Xu, G. Q. Liu, Y. J. Fu, Z. Liu, X. J. Tan, H. Z. Shao, H. C. Jiang, T. Y. Tan, J. Jiang, *Appl. Phys. Lett.* **2016**, *108*, 083902.
[13] PDF-2 Release 2008, Joint Committee on Powder Diffraction Standards (JCPDS)-International Centre for Diffraction Data (ICDD), **2008**.
[14] D. D. Vaughn, S. I. In, R. E. Schaak, *ACS Nano* **2011**, *5*, 8852.
[15] B. Z. Sun, Z. J. Ma, C. He, K. C. Wu, *Phys. Chem. Chem. Phys.* **2015**, *17*, 29844.
[16] S. I. Kim, S. Hwang, S. Y. Kim, W. J. Lee, D. W. Jung, K. S. Moon, H. J. Park, Y. J. Cho, Y. H. Cho, J. H. Kim, D. J. Yun, K. H. Lee, I. T. Han, K. Lee, Y. Sohn, *Sci. Rep.* **2016**, *6*, 19733.
[17] D. Feng, Z.-H. Ge, D. Wu, Y.-X. Chen, T. Wu, J. Li, J. He, *Phys. Chem. Chem. Phys.* **2016**, *18*, 31821.
[18] a) T. T. X. Vo, T. N. H. Le, Q. N. Pham, C. Byl, D. Dragoe, M. G. Barthes-Labrousse, D. Berardan, N. Dragoe, *Phys. Status Solidi A* **2015**, *212*, 2776; b) K. Rubenis, S. Populoh, P. Thiel, S. Yoon, U. Müller, J. Locs, *J. Alloys Compd.* **2017**, *692*, 515.
[19] D. Martinez-Escobar, M. Ramachandran, A. Sanchez-Juarez, J. S. N. Rios, *Thin Solid Films* **2013**, *535*, 390.
[20] S. Saha, A. Banik, K. Biswas, *Chem. - Eur. J.* **2016**, *22*, 15634.
[21] a) A. C. Larson, R. B. Von Dreele, *General Structure Analysis System (GSAS), Los Alamos National Laboratory Report LAUR 86-748*, Los Alamos National Laboratory, Los Alamos, NM **1994**; b) B. H. Toby, *J. Appl. Crystallogr.* **2001**, *34*, 210.

